Spin friction in two-dimensional antiferromagnetic crystals

Yao Li and Wanlin Guo[*]

Key Laboratory for Intelligent Nano Materials and Devices of MOE and State Key Laboratory of Mechanics and Control for Mechanical Structures, Nanjing University of Aeronautics and Astronautics, Nanjing 210016, China

The spin-state-dominated frictional force and stick-slip behaviors are shown through first-principles calculations using Mn_2C, a two-dimensional antiferromagnetic crystal, as a prototype. While the frictional force in the spin-unpolarized state is isotropic and independent with forward and backward moving directions, the antiferromagnetic ordering not only reduces the rotational symmetries of potential energy surfaces, but also dramatically changes the shapes of energy landscapes on the energetically preferred sliding paths, leading to anisotropic and even direction-dependent frictional force. Besides, a novel stick-slip behavior with the slips occurring across a fractional number of lattice sites is observed and the transition conditions of the stick-slip behavior can be predicted by the Tomlinson model.

I. INTRODUCTION

The classic friction law loses its dominance at nanoscale where the contributions from phononic and electronic interactions become significant, even quantum fluctuations may play a significant role [1–5]. Experimentally, atomic force microscopes are widely employed to study atomic-scale friction, which can scan a nanoscale tip over atomically flat surfaces and measure the lateral force by a cantilever spring holding the tip [6]. By scanning the graphite surface with a tungsten tip, Mate *et al.* observed an atomic-scale stick-slip behavior, where the lateral force shows a sawtoothlike modulation due to the sticking and subsequent rapid slip of the tip [7]. When the load is sufficiently low, the stick-slip behavior can translate into continuous sliding [8], otherwise the slips have periodicities of a single or an integer number of lattice sites, identified as "single slip" or "multiple slip" and revealed in the framework of the Tomnlinson model [9–12]. Based on spin exchange interactions, a magnetic tip can be employed to resolve the spin structures of magnetic surfaces [13]. The friction caused by the relative motion between the magnetic tip and the magnetic surface is affected by spin degrees of freedom, and so has been denoted as spin or magnetic friction [14,15]. Using a spin-polarized scanning tunneling microscope in combination with Monte Carlo simulations, Wolter *et al.* studied the friction of a single Co atom moving over a Mn/W(110) surface and showed the stick-slip behaviors of spin friction, indicating that the spin degree of freedom must be taken into account in the friction of magnetic systems [16]. Recently, Ouazi *et al.* found that the signal of surface spin textures can be amplified by the spin frictions between a magnetic adatom and a magnetic surface [17]. However, the origin of spin friction and the transition conditions of the spin frictional behaviors are still elusive. Besides, as antiferromagnetic spin ordering can break the lattice symmetry, the frictional behaviors in antiferromagnetic crystals must change.

Due to the natural surfaces, two-dimensional (2D) crystals have been used as ideal platforms to reveal unusual electronic, optical, and mechanical properties [18–20]. But few researches focused on the interlayer magnetic interaction due to the rareness of 2D crystals with long range magnetic ordering. Recently, 2D antiferromagnetism and ferromagnetism have been revealed at low temperature by Raman and magneto-optic Kerr microscopy, respectively [21–23]. Different from nonmagnetic 2D crystals where the van der Waals (vdW) force dominates the interlayer interaction, the interlayer spin exchange interaction is proved significant for these 2D magnetic crystals [21–23]. Theoretically, several room-temperature 2D magnetic crystals have been predicted [24–26]. Among them, 2D antiferromagnetic Mn_2C has large magnetic moments, high Néel temperature, and an h-MoS_2-like structure [24], which could induce large interlayer spin friction.

In the present work, we find that the spin degree of freedom dominates the interlayer frictional force and stick-slip behaviors of 2D antiferromagnetic Mn_2C. Employing first-principles calculation together with the Ising model, it is shown that the antiferromagnetic ordering reduces the rotational symmetries of the potential energy surfaces (PESs) and induces anisotropic, nonsinusoidal, and even asymmetrical energy landscapes on minimum energy paths (MEPs). The corresponding frictional forces and stick-slip behaviors derived from the Tomlinson model [9] are also anisotropic and even different in forward and backward moving directions. On the MEPs with nonsinusoidal energy landscapes, a novel stick-slip behavior with slips across a fractional number of lattice sites is observed in a certain range of spring stiffness and the transitions conditions from this "fractional slip" to multiple slip are predicted.

II. METHODS

The first-principles calculations are performed within the framework of density functional theory (DFT) as implemented in the VASP code [27,28]. The generalized gradient

———————
[*]wlguo@nuaa.edu.cn
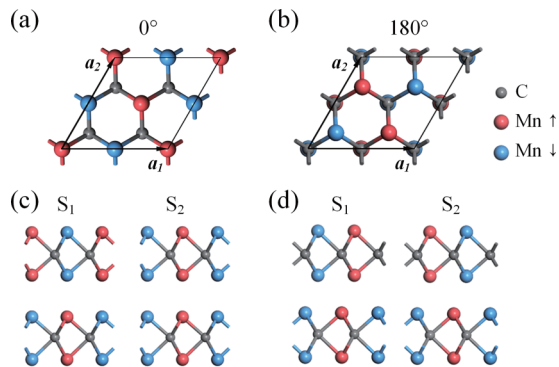
FIG. 1. The 2×2 supercell cell and spin ordering of bilayer Mn$_2$C with (a) and (c) $0°$ and (b) and (d) $180°$ stacking angles. (a) and (b) Top views and (c) and (d) side views. The gray ball represents the C atom and the red and blue balls represent Mn atoms with spin-up and spin-down directions, respectively. S_1 and S_2 mark the two initial spin states.

approximation in the form of the Perdew-Burke-Ernzerhof exchange correlation functional and projector augmented wave potentials are employed [29–31]. The DFT-D2 method is used for the corrections of vdW interactions [32]. The GGA + U method is adopted for strong-correlated correction of Mn's 3d electrons, with U and J set to be 4.0 and 1.0 eV, respectively [24]. The kinetic energy cutoff is adopted to be 450 eV and the reciprocal space is meshed at $21 \times 21 \times 1$. The energy and force convergence criteria are set to be 10^{-6} eV and 0.01 eV/Å, respectively.

A 2D Mn$_2$C monolayer has an h-MoS$_2$-like structure and the antiferromagnetism is attributed to the surface Mn atoms. So a 2×2 supercell is employed in all calculations with the optimized lattice constant a_0 of 5.12 Å. When two Mn$_2$C layers are stacked, the in-plane antiferromagnetic ordering does not change no matter what type of interlayer spin ordering. To investigate how the interlayer interaction changed with different stacking angles and positions, we considered the stackings with the upper layer rotated by $0°$ and $180°$, and defined two initial spin states S_1 and S_2 for the initial stackings AA (eclipsed with Mn over Mn and C over C) and AA' (eclipsed with Mn over C) as shown in Fig. 1. The difference between S_1 and S_2 is the spin directions in the upper layer, and after translating $1/2 \times \vec{a}_1$ or $1/2 \times \vec{a}_2$, S_1 is identical with S_2. Then the upper layer is moved step by step along the lattice vectors $\vec{a}_1$ and $\vec{a}_2$. The interlayer distance was fully optimized after each movement to keep the external normal force always equal to zero. So the friction is induced by the interlayer interaction. The resulting interlayer distance varies from 0.23 to 0.26 nm as shown in Figs. S1(b) and S1(d) in the Supplemental Material [38]. The fractional coordinate of $\vec{a}_1$ and $\vec{a}_2$ was used to mark the movement of the upper layer.

III. RESULTS AND DISCUSSION

Before considering the interlayer spin couplings, spin-unpolarized calculations were carried out. At $0°$ stacking, the PES of nonmagnetic state has a sixfold rotational symmetry. AA and AB (staggered with Mn over C) stackings have the highest and lowest total energies, respectively, as shown in
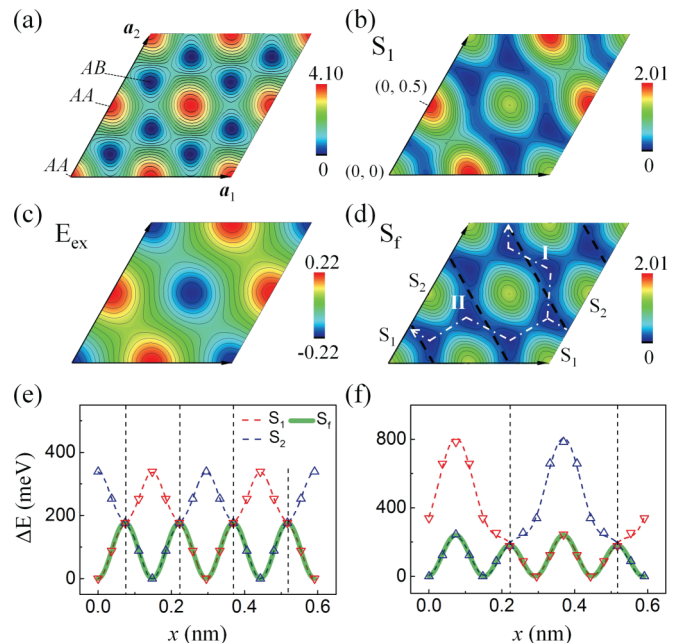
FIG. 2. Potential energy surfaces of nonmagnetic (a), S_1 (b), and S_f (d) states at $0°$ stacking, and the corresponding interlayer exchange energy surface of S_1 state (c). The black dashed lines represent the frustration states. The white dash-dotted lines represent the two minimum energy paths along I and II directions and the details are shown in (e) and (f), respectively. The unit of the scalar bar is eV/supercell.

Fig. 2(a). When the upper Mn$_2$C layer is rotated by $180°$, AB' stacking (staggered with C over C) is nonequivalent with AA' stacking and the rotational symmetry of PES reduces to threefold [see Fig. 3(a)]. $A'B$ stacking (staggered with Mn over Mn) has the highest energy, while AA' stacking has the lowest energy. For both $0°$ and $180°$, except with a larger energy corrugation attributed to the strong chemical potential, the shapes of PESs are similar to other hexagonal crystals such as graphene, BN, and MoS$_2$ [33–36], so similar frictional behaviors can be expected. But the PESs remarkably changed when considered the spin polarization.

First, we consider the S_1 state at $0°$ stacking. The symmetry of the PES reduces to twofold and the length of potential periods doubles due to the in-plane antiferromagnetic ordering [see Fig. 2(b)]. For example, (0,0) and (0,0.5) are both AA stackings but the interlayer spin couplings of them are antiferromagnetic and ferromagnetic, respectively. And (0, 0) has an obviously lower energy.

To identify the role of the spin degree of freedom, we employed the Ising model for a two-dimensional hexagonal lattice with pairwise exchange constant $J_0 < 0$ [16,37]. Here we only consider the two contacted Mn atom layers with an estimated interlayer distance of 2.4 Å based on the results of DFT. The Hamiltonian can be written as

$$H_{ex} = -\sum_{i \in up} \sum_{\substack{j \in bott \\ r_{ij} < r_{cut}}} J(r_{ij}) S_i S_j, \qquad (1)$$

where i and j denote the Mn atoms in upper and bottom layers, respectively, and the exchange constant is assumed
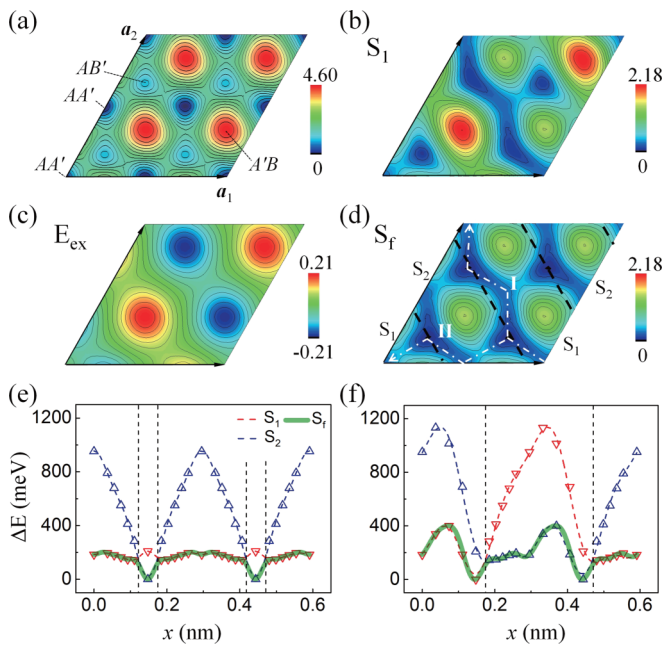
FIG. 3. Potential energy surfaces of nonmagnetic (a), S_1 (b), and S_f (d) states at 180° stacking, and the corresponding interlayer exchange energy surface of S_1 state (c). The black dashed lines represent the frustration states. The white dash-dotted lines represent the two minimum energy paths along I and II directions and the details are shown in (e) and (f), respectively. The unit of the scalar bar is eV/supercell.

with exponential decay $J(r_{ij}) = J_0 e^{\gamma_0(r_{ij}-r_0)}$ (r_{ij} is the distance between atoms i and j while γ_0 and r_0 are constants as listed in Table SI [38]). The interlayer exchange energy surface of S_1 is shown in Fig. 2(c) and it has the same rotational symmetry and period length as the PES. The exchange energy can be positive or negative depending on the directions of the interacting spins. So, while the stacking structure determines interlayer chemical and vdW interactions, the magnetic structure modifies the shapes of PESs by interlayer exchange interaction. The estimated energy corrugation of interlayer exchange energy is larger than that of vdW energy (see Fig. S1 [38]) but only accounts for 21% of the total energy corrugation.

The PES of spin state S_2 has a phase difference of $1/2 \times \vec{a}_1$ (see Fig. S2 [38]). To obtain the ground state energy at each position, we define the energy minimum of S_1 and S_2 in each step as S_f, representing the spin flip in moving [see Fig. 2(d)]. The black dashed lines in the PES of S_f separate the regions of S_1 and S_2. The points on the black dashed lines are magnetic frustration states where the energies of S_1 and S_2 are equal. The white dot-dashed lines in Fig. 2(d) represent the MEPs along I and II directions, respectively. Both of the paths pass through the lowest-energy stacking, but the frequency of passing through the magnetic frustration states in I direction is two times as that in II direction as shown in Figs. 2(e) and 2(f). In 2D vdW crystals, the energy landscapes on MEPs at 0° usually can be fitted well by sinusoid. Here, except for the S_f state on path I, the energy landscapes are all nonsinusodial attributed to the interlayer exchange interaction. We employed the Fourier series $f(x) = \sum_{k=0}^{n} E_k/2 \cos(2k\pi x/a + \phi_k)$ with $2 \leqslant n \leqslant 4$ to fit the energy landscapes, where E_k and ϕ_k are
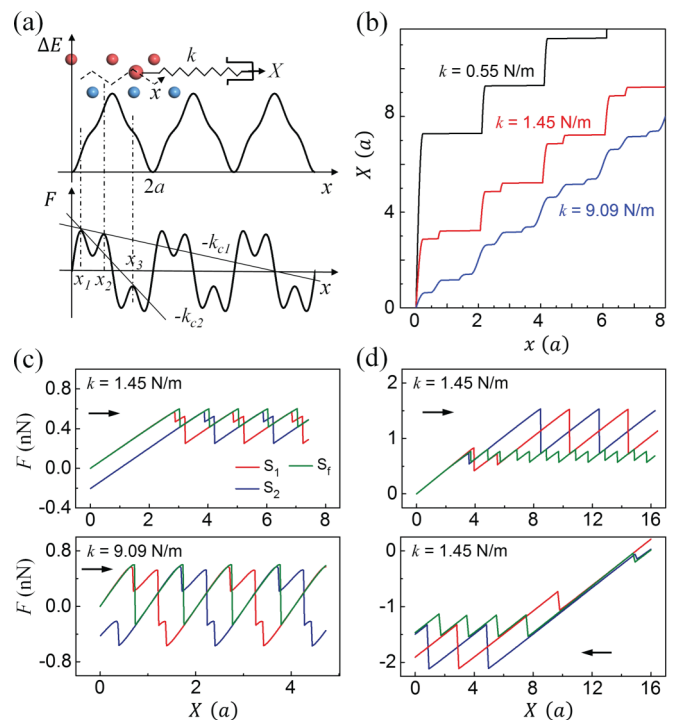
FIG. 4. (a) The periodic potential and interlayer interaction force at 0° path I. The inset shows the system configuration and, except for one spin-up Mn atom, the other atoms in the upper layer are not shown. (b) The relation between the displacements of the upper layer x and the support X at different spring stiffnesses k. The relations between the frictional force F and the movement of support X at 0° path I (c) and 180° path II (d). The arrow represents moving direction.

the component of energy corrugation and phase difference, respectively. $a = a_0/2\sqrt{3}$ is the in-plane component of the distance between two nearest lattice sites. The number of terms used and the R-square of each fitting are listed in Table SII in the Supplemental Materials [38].

The PESs of spin-polarized states at 180° stacking are similar but have only onefold rotational symmetries as shown in Fig. 3. It is interesting that on the PES of S_f, AB' stacking becomes the lowest-energy stacking. On path I [Fig. 3(e)], the energy corrugation of S_1 is lower than that of S_f. Besides, the energy landscape on path II [see Fig. 3(f)] are all asymmetrical: $f(x+c) \neq f(-x+c)$, where c is an arbitrary constant. The energy landscape are also fitted by the Fourier series, but with $3 \leqslant n \leqslant 5$ due to the decrease of symmetry.

From the above analyses, we conclude that: (i) the energy landscapes on MEPs are anisotropic and have lower energy corrugations in I direction; and (ii) the weak interlayer exchange interaction can dramatically change the energy landscapes by introducing high order energy terms, reducing symmetry and changing the lowest-energy stacking, and finally affect the frictional behavior.

To study the stick-slip behaviors, we employed the Tomlinson model with the energy landscapes fitted above [see Fig. 4(a)], and the effective potential is written as

$$V = f(x) + \frac{1}{2}k(x-X)^2, \quad (2)$$

where k and X are the effective spring constant and the displacement of the moving support, respectively [9,39]. The equation of force equilibrium for the upper layer is $\partial V/\partial(x) = 0$, thus

$$F = -k(x - X) = \frac{\partial f(x)}{\partial x}, \qquad (3)$$

where F is the interlayer interaction force.

The stick-slip behaviors on the MEPs with nonsinusoidal energy landscapes are totally different. Taking the $0°$ path I of S_1 state as an example, the derivative of the potential function has three local maximums at x_1, x_2, and x_3 in one period with $\partial f(x_1)/\partial x > \partial f(x_2)/\partial x > \partial f(x_3)/\partial x$ [see Fig. 4(a)]. The tangent lines represent the spring forces and the absolute values of the slops k_{c1} and k_{c2} are critical spring stiffnesses.

As the periodicity of the potential equals to $2a$, the upper layer only sticks near x_1 and slips across two lattice sites when the spring stiffness k is small. When $k_{c1} \leqslant k \leqslant k_{c2}$, the force in the spring decreases faster and the upper layer sticks not only near x_1 but also near x_2. So the slip across two lattice sites splits into two slips with different lengths and the other local maximum frictional force equals to $\partial f(x_2)/\partial x$. Different from the "double slip" or "multiple slip" which refers to a slip through two or an integer number of lattice sites [8,11,12], the slip here occurs across a fractional number of lattice sites and we name this behavior by "i/j slip" or "2/2 slip," representing j "fractional slips" across i lattice sites, where i and j are integers. When $k \geqslant k_{c2}$, a new stick position x_3 occurs and there are three fractional slips across two lattice sites, called "2/3 slip." The critical spring stiffness k_{c1} of the transition from double slip to 2/2 slip can be estimated: $k_{c1} = [\partial f(x_1)/\partial x - \partial f(x_2)/\partial x]/(x_2 - x_1)$. k_{c2} for 2/3 slip can be derived analogously. Figure 4(b) shows the relation between the displacements of the upper layer x and the support X of double, 2/2, and 2/3 slips, where the platforms on the curves represent the slips of the upper layer. The relations between the frictional force F and X for 2/2 and 2/3 slips are shown in Fig. 4(c). The initial negative force of S_2 state occurs because it starts from a high energy position. The frictional forces on other paths are shown in Fig. S3 [38].

When k further increases, one slip first translates into continuous sliding while other slips are kept. Using the strategy proposed by Socoliuc *et al.* for single slip [8], the critical stiffness value of a transition from each fractional slip to continuous sliding can be obtained, $k_i = [\partial^2 f(x)/\partial x^2]_{max}$, where k_i is the ith local maximum values. Finally, all of the slips will completely translate into continuous sliding. From Eq. (3), we can find that the maximum value of frictional force F_{max} is proportional to the maximum value of $\partial f(x)/\partial x$, so under different spin states, the frictional forces are dramatically different. On the paths with sinusoidal energy landscape $f(x) = E_1/2 \cos(2\pi x/a)$, it can be derived that

$(\partial f(x)/\partial x)_{max} = E_1$, so the amount of F_{max} is proportional to the energy corrugation E_1. But for the energy landscapes fitted by the Fourier series with $n \geqslant 2$, the value of $[\partial f(x)/\partial x]_{max}$ must be considered. For example, at $0°$ path I, the energy corrugation of S_1 is much larger than that of S_f state, but the frictional force of S_1 is smaller, as shown in Fig. 4(c). For symmetrical energy landscape $f(x + c) = f(-x + c)$, the frictional forces are the same in both x and $-x$ directions. But for asymmetrical energy landscape on $180°$ path II, $\partial f(x)/\partial x \neq \partial f(-x)/\partial(-x)$, so both the values of F_{max} and the stick-slip behaviors are different [see Fig. 4(d)], showing the direction-dependent friction.

Considering the dynamic details of spin flip and the thermal effects would be useful but still challenging in the framework of DFT. The spin flip time t_s in Mn compounds ranges from 10^{-12} to 10^{-1} s [40,41]. The scanning speed of atomic force microscopy can be 10^0 to 10^5 nm/s [42], so the time of scanning over one lattice site t_l can be estimated as 10^{-6} to 10^1 s. When $t_s \ll t_l$, spin would fully relax and the frictional force should equal the force in S_f state. When $t_s \gg t_l$, the frictional force should be estimated as the force in S_1 or S_2 state. But when $t_s \approx t_l$, the dynamics of spin coupled with vdW and chemical interactions must be taken into account. Beside, high magnetic fields can change the in-plane antiferromagnetism to ferromagnetism, then the frictional behaviors here will totally change.

IV. CONCLUSION

In conclusion, we revealed the spin dominated friction between layers of 2D antiferromagnetic Mn_2C based on first-principles calculations and the Tomlinson model. The interlayer exchange interactions between the in-plane antiferromagnetic orderings dramatically change the shapes of energy landscapes, leading to direction-dependent frictions and a novel stick-slip behavior with slips across a fractional number of lattice sites. This deepened understanding of spin frictional behavior should shed light on developing spin-related devices and techniques such as the high-performance magnetic disk and noncontact motion control technique.

[1] M. S. Tomassone and A. Widom, Phys. Rev. B **56**, 4938 (1997).

[2] Q. Li, Y. Dong, D. Perez, A. Martini, and R. W. Carpick, Phys. Rev. Lett. **106**, 126101 (2011).

[3] Z. Tshiprut, S. Zelner, and M. Urbakh, Phys. Rev. Lett. **102**, 136102 (2009).

[4] M. S. Tomassone, J. B. Sokoloff, A. Widom, and J. Krim, Phys. Rev. Lett. **79**, 4798 (1997).

[5] J. B. Pendry, J. Phys.: Condens. Matter **9**, 10301 (1997).

[6] G. Binnig, C. F. Quate, and C. Gerber, Phys. Rev. Lett. **56**, 930 (1986).

[7] C. M. Mate, G. M. McClelland, R. Erlandsson, and S. Chiang, Phys. Rev. Lett. **59**, 1942 (1987).

[8] A. Socoliuc, R. Bennewitz, E. Gnecco, and E. Meyer, Phys. Rev. Lett. **92**, 134301 (2004).

[9] G. Tomlinson, Philos. Mag. **7**, 905 (1929).

[10] D. Tománek, W. Zhong, and H. Thomas, Europhys. Lett. **15**, 887 (1991).

[11] J. Nakamura, S. Wakunami, and A. Natori, Phys. Rev. B **72**, 235415 (2005).

[12] S. N. Medyanik, W. K. Liu, I.-H. Sung, and R. W. Carpick, Phys. Rev. Lett. **97**, 136106 (2006).

[13] R. Wiesendanger, Rev. Mod. Phys. **81**, 1495 (2009).

[14] C. Fusco, D. E. Wolf, and U. Nowak, Phys. Rev. B **77**, 174426 (2008).

[15] D. Kadau, A. Hucht, and D. E. Wolf, Phys. Rev. Lett. **101**, 137205 (2008).

[16] B. Wolter, Y. Yoshida, A. Kubetzka, S.-W. Hla, K. von Bergmann, and R. Wiesendanger, Phys. Rev. Lett. **109**, 116102 (2012).

[17] S. Ouazi, A. Kubetzka, K. von Bergmann, and R. Wiesendanger, Phys. Rev. Lett. **112**, 076102 (2014).

[18] A. K. Geim and I. V. Grigorieva, Nature (London) **499**, 419 (2013).

[19] A. M. Jones, H. Yu, J. S. Ross, P. Klement, N. J. Ghimire, J. Yan, D. G. Mandrus, W. Yao, and X. Xu, Nat. Phys. **10**, 130 (2014).

[20] M. Dienwiebel, G. S. Verhoeven, N. Pradeep, J. W. M. Frenken, J. A. Heimberg, and H. W. Zandbergen, Phys. Rev. Lett. **92**, 126101 (2004).

[21] C. Gong, L. Li, Z. Li, H. Ji, A. Stern, Y. Xia, T. Cao, W. Bao, C. Wang, Y. Wang *et al.*, Nature (London) **546**, 265 (2017).

[22] B. Huang, G. Clark, E. Navarro-Moratalla, D. R. Klein, R. Cheng, K. L. Seyler, D. Zhong, E. Schmidgall, M. A. McGuire, D. H. Cobden *et al.*, Nature (London) **546**, 270 (2017).

[23] X. Wang, K. Du, Y. Y. F. Liu, P. Hu, J. Zhang, Q. Zhang, M. H. S. Owen, X. Lu, C. K. Gan, P. Sengupta *et al.*, 2D Mater. **3**, 031009 (2016).

[24] L. Hu, X. Wu, and J. Yang, Nanoscale **8**, 12939 (2016).

[25] Y. Sun, Z. Zhuo, X. Wu, and J. Yang, Nano Lett. **17**, 2771 (2017).

[26] B. L. Chittari, Y. Park, D. Lee, M. Han, A. H. MacDonald, E. Hwang, and J. Jung, Phys. Rev. B **94**, 184428 (2016).

[27] G. Kresse and J. Furthmüller, Phys. Rev. B **54**, 11169 (1996).

[28] G. Kresse and J. Hafner, Phys. Rev. B **47**, 558 (1993).

[29] P. E. Blöchl, Phys. Rev. B **50**, 17953 (1994).

[30] G. Kresse and D. Joubert, Phys. Rev. B **59**, 1758 (1999).

[31] J. P. Perdew, K. Burke, and M. Ernzerhof, Phys. Rev. Lett. **77**, 3865 (1996).

[32] S. Grimme, J. Comput. Chem. **27**, 1787 (2006).

[33] M. Reguzzoni, A. Fasolino, E. Molinari, and M. C. Righi, Phys. Rev. B **86**, 245434 (2012).

[34] Y. Guo, W. Guo, and C. Chen, Phys. Rev. B **76**, 155429 (2007).

[35] G. Constantinescu, A. Kuc, and T. Heine, Phys. Rev. Lett. **111**, 036104 (2013).

[36] G. Levita, A. Cavaleiro, E. Molinari, T. Polcar, and M. Righi, J. Phys. Chem. C **118**, 13809 (2014).

[37] T. D. Schultz, D. C. Mattis, and E. H. Lieb, Rev. Mod. Phys. **36**, 856 (1964).

[38] See Supplemental Material at http://link.aps.org/supplemental/10.1103/PhysRevB.97.104302 for the surfaces of vdW energy and interlayer distance; the PES of S_2 state; the frictional force on other paths; the parameters used in the Ising model; and the details of the fitting of MEPs.

[39] L. Prandtl, Angew. Math. Mech. **8**, 85 (1928).

[40] G. Bastard and L. L. Chang, Phys. Rev. B **41**, 7899 (1990).

[41] M. Goryca, T. Kazimierczuk, M. Nawrocki, A. Golnik, J. A. Gaj, P. Kossacki, P. Wojnar, and G. Karczewski, Phys. Rev. Lett. **103**, 087401 (2009).

[42] X. Z. Liu, Z. Ye, Y. Dong, P. Egberts, R. W. Carpick, and A. Martini, Phys. Rev. Lett. **114**, 146102 (2015).